SN 2016jhj at redshift 0.34: extending the Type II supernova Hubble diagram using the standard candle method

T. de Jaeger[1]★, L. Galbany[2], A. V. Filippenko[1,3], S. González-Gaitán[4,5], N. Yasuda[6],
K. Maeda[6,7], M. Tanaka[6,8] T. Morokuma[6,9], T. J. Moriya[8], N. Tominaga[6,10],
K. Nomoto[6], Y. Komiyama[11,12], J. P. Anderson[13], T. G. Brink[1], R. G. Carlberg[14],
G. Folatelli[15,6], M. Hamuy[16,5], G. Pignata[17,5], W. Zheng[1]

[1]*Department of Astronomy, University of California, Berkeley, CA 94720-3411, USA.*
[2]*PITT PACC, Department of Physics and Astronomy, University of Pittsburgh, Pittsburgh, PA 15260, USA.*
[3]*Senior Miller Fellow, Miller Institute for Basic Research in Science, University of California, Berkeley, CA 94720, USA.*
[4]*Center for Mathematical Modelling, University of Chile, Beauchef 851, Santiago, Chile.*
[5]*Millennium Institute of Astrophysics (MAS), Nuncio Monseñor Sótero Sanz 100, Providencia, Santiago, Chile.*
[6]*Kavli Institute for the Physics and Mathematics of the Universe (WPI), The University of Tokyo, 5-1-5 Kashiwanoha, Kashiwa, Chiba 277-8583,*
[7]*Department of Astronomy, Kyoto University, Kitashirakawa-Oiwake-cho, Sakyo-ku, Kyoto, 606-8502, Japan.*
[8]*Division of Theoretical Astronomy, National Astronomical Observatory of Japan, Tokyo 181-8588, Japan.*
[9]*Institute of Astronomy, The University of Tokyo, Mitaka, Tokyo 181-0015, Japan.*
[10]*Department of Physics, Faculty of Science and Engineering, Konan University, 8-9-1 Okamoto, Kobe, Hyogo 658-8501, Japan.*
[11]*National Astronomical Observatory of Japan, 2-21-1 Osawa, Mitaka, Tokyo 181-8588, Japan.*
[12]*Graduate University for Advanced Studies (SOKENDAI), 2-21-1 Osawa, Mitaka, Tokyo 181-8588, Japan.*
[13]*European Southern Observatory, Alonso de Córdova 3107, Casilla 19, Santiago.*
[14]*Department of Astronomy and Astrophysics, University of Toronto, 50 St. George St., Toronto, ON, M5S 3H4, Canada.*
[15]*Facultad de Ciencias Astronómicas y Geofísicas, UNLP, IALP, CONICET, Paseo del Bosque S/N, B1900FWA La Plata, Argentina.*
[16]*Departamento de Astronomía – Universidad de Chile, Camino el Observatorio 1515, Santiago, Chile.*
[17]*Departamento de Ciencias Fisicas, Universidad Andres Bello, Avda. Republica 252, Santiago, Chile.*

ABSTRACT

Although Type Ia supernova cosmology has now reached a mature state, it is important to develop as many independent methods as possible to understand the true nature of dark energy. Recent studies have shown that Type II supernovae (SNe II) offer such a path and could be used as alternative distance indicators. However, the majority of these studies were unable to extend the Hubble diagram above redshift $z = 0.3$ because of observational limitations. Here, we show that we are now ready to move beyond low redshifts and attempt high-redshift ($z \gtrsim 0.3$) SN II cosmology as a result of new-generation deep surveys such as the Subaru/Hyper Suprime-Cam (HSC) survey. Applying the "standard candle method" to SN 2016jhj ($z = 0.3398 \pm 0.0002$; discovered by HSC) together with a low-redshift sample, we are able to construct the highest-redshift SN II Hubble diagram to date with an observed dispersion of 0.27 mag (i.e., 12–13% in distance). This work demonstrates the bright future of SN II cosmology in the coming era of large, wide-field surveys like that of the Large Synoptic Survey Telescope.

Key words: cosmology: distance scale – galaxies: distances and redshifts – stars: supernovae: general

1 INTRODUCTION

Type Ia supernovae (SNe Ia; Minkowski 1941; Filippenko 1997, and references therein) are good standardisable can-

★ E-mail: tdejaeger@berkeley.edu

dles (e.g., Phillips 1993; Hamuy et al. 1996; Riess et al. 1996; Perlmutter et al. 1997) that allow measurement of extragalactic distances with an accuracy of $\sim 5\%$ (e.g., Betoule et al. 2014; Rubin & Hayden 2016). They play a crucial role in the determination of the expansion rate of the Universe (Riess et al. 2016, and references therein), and in 1998 they revealed the surprising accelerated growth rate of the Universe driven by an unknown effect attributed to dark energy (Riess et al. 1998; Schmidt et al. 1998; Perlmutter et al. 1999). However, even though SNe Ia remain the most mature and well-exploited method measuring the acceleration, further improvement to constrain the nature of dark energy requires developing as many independent methods as possible.

Among the wide range of independent cosmological probes found in the literature such as the cosmic microwave background radiation (Fixsen et al. 1996; Jaffe et al. 2001; Spergel et al. 2007; Bennett et al. 2003; Planck Collaboration et al. 2013), baryon acoustic oscillations (Blake & Glazebrook 2003; Seo & Eisenstein 2003), X-ray clusters (White et al. 1993; Schuecker et al. 2003), and superluminous SNe (Inserra & Smartt 2014), one interesting independent method for deriving accurate distances and measuring cosmological parameters is Type II SNe[1].

Observationally, SNe II are characterised by the presence of strong hydrogen (H) features in their spectra (see, e.g., Filippenko 2000 and Filippenko 1997 for overviews), and a plateau of varying steepness in their light curves (Barbon et al. 1979). Even though detecting SNe II at high redshift is challenging owing to their relatively low luminosity (1–2 mag fainter than SNe Ia; Richardson et al. 2014), their use as cosmic distance indicators is motivated by the fact that they are more abundant than SNe Ia (Li et al. 2011); additionally, their rate is expected to peak at higher redshifts than that of SNe Ia (Taylor et al. 2014; Cappellaro et al. 2015). Also, thanks to direct progenitor detections and hydrodynamical models (Van Dyk et al. 2003; Smartt et al. 2009; Grassberg et al. 1971; Falk & Arnett 1977; Chevalier 1976), their progenitors and environments (only late-type galaxies) are better understood than those of SNe Ia (no direct progenitor detection and found also in elliptical galaxies, not just late-type galaxies). It is now accepted that their progenitors are red supergiants that have retained a significant fraction of their H envelopes. Unlike SNe Ia, for which possible redshift evolution is debated (Kessler et al. 2009; Guy et al. 2010; Betoule et al. 2014), SN II progenitors have been constrained, and the explosion mechanism is better understood (Woosley & Weaver 1995; Janka et al. 2007).

At first sight, the SN II family displays a large range of peak luminosities; however, as for SNe Ia, their extrinsic differences such as dust extinction can be calibrated. To date, several methods have been developed to standardise SNe II, such as the expanding photosphere method (EPM; Kirshner & Kwan 1974), the standard candle method (SCM; Hamuy & Pinto 2002), the photospheric magnitude method (PMM;

Rodríguez et al. 2014), and the most recent technique based solely on photometric inputs called the photometric colour method (PCM; de Jaeger et al. 2015, 2017). In this paper, we focus our effort on the SCM, which is the most common method used to derive SN II distances, and currently the most accurate. The SCM is a powerful method based on both photometric and spectroscopic input parameters which enables a decrease of the scatter in the Hubble diagram from ~ 1 mag (with calibration) to levels of ~ 0.3 mag (Hamuy & Pinto 2002), equivalent to a precision of $\sim 14\%$ in distances. This method is mainly built on the observed correlation between SN II luminosity and photospheric expansion velocity ~ 50 days post-explosion: more luminous SNe II have higher velocities (Hamuy & Pinto 2002). The underlying physical cause of this empirical relation (Kasen & Woosley 2009) is that in more-luminous SNe II the H recombination front defining the photosphere is farther out in radius, and therefore maintained at higher velocities because of homologous expansion.

Currently, refined versions of the SCM combine the velocity ejecta correction measured through the absorption minimum of P-Cygni features (Fe II λ5169 or Hβ λ4861 lines) with a dust correction based on the SN II colour. Using this fine-tuned method, recent works succeeded in constructing a Hubble diagram with a dispersion of ~ 10–12% in distance (Nugent et al. 2006; Poznanski et al. 2009; Olivares E. et al. 2010; D'Andrea et al. 2010; de Jaeger et al. 2015, 2017), and provide new independent evidence for dark energy at the level of 2σ (de Jaeger et al. 2017). Even if SNe II are currently not competitive with SNe Ia in terms of achieved dispersion (~ 0.25 mag versus ~ 0.10 mag) or sample size (~ 60 SNe II versus ~ 740 SNe Ia), the latest SN II studies are comparable to the early SN Ia results, showing that SNe II are a useful complementary and independent method to constrain the nature of dark energy.

Nevertheless, all SN II Hubble diagrams based on the SCM found in the literature used relatively low-redshift samples ($z \lesssim 0.2$), except the recent work done by Gall et al. (2017) where the authors used one SN II at a redshift of 0.335. At low redshift, the differences between the expansion histories are extremely small, and distinguishing among the different cosmological models requires measurements extending far back in time: SNe II at higher redshift (at least $z \approx 0.3$–0.5). Here, as proof of concept, we show our ability to extend the current SN II Hubble diagram beyond $z = 0.3$, taking advantage of the Subaru/Hyper Suprime-Cam survey (HSC; Miyazaki et al. 2012; Aihara et al. 2017) and using different methodologies than those used by Gall et al. (2017).

This work also addresses the critical issue of the necessity for the community to dedicate more observations of high-redshift SNe II in order to directly compare with SN Ia results. This could be achieved with new, deep surveys (e.g., the Large Synoptic Survey Telescope, LSST: Ivezić et al. 2009; HSC: Miyazaki et al. 2012; Aihara et al. 2017) and ground-base telescopes for spectroscopy such as the Keck telescopes or the next generation of 25–39 m telescopes (European Extremely Large Telescope, E-ELT: Gilmozzi & Spyromilio 2007; Giant Magellan Telescope, GMT: Johns et al. 2012; Thirty Meter Telescope, TMT: Sanders 2013).

This paper is organised as follows. Section 2 contains a description of the data sample, and in Section 3 we discuss the method used to derive the Hubble diagram, which differs

---

[1] Throughout this paper, SNe II refer collectively to the two historical groups, SNe IIP and SNe IIL, since recent studies show that the SN II family forms a relatively continuous class (Anderson et al. 2014; Sanders et al. 2015; Valenti et al. 2016; Galbany et al. 2016).

from that of de Jaeger et al. (2017). In Section 4 we discuss our results, and Section 5 summarised our conclusions.

2 DATA SAMPLE

Here we use the sample from de Jaeger et al. (2017), which consist of SNe II from three different projects: the Carnegie Supernova Project[2] (CSP-I; Hamuy et al. 2006), the SDSS-II SN Survey[3] (Frieman et al. 2008), and the Supernova Legacy Survey[4] (Astier et al. 2006; Perrett et al. 2010). We complete the sample with SN 2016jhj, a recently discovered high-redshift SN II from the HSC (Aihara et al. 2017).

2.1 CSP-I+SDSS+SNLS

A list of 82 SNe II available for the SCM was compiled by de Jaeger et al. (2017). Among this sample, 61 low-redshift SNe II are from the CSP-I (Anderson et al., in prep.), 16 from the SDSS (D'Andrea et al. 2010), and 5 from the SNLS (unpublished data). For more information about the different surveys and data-reduction procedures, the reader is referred to D'Andrea et al. (2010), de Jaeger et al. (2017), and references therein.

All of the magnitudes were simultaneously corrected for Milky Way extinction (A_V G; Schlafly & Finkbeiner 2011), the expansion of the Universe (K-correction; Oke & Sandage 1968; Hamuy et al. 1993; Kim et al. 1996; Nugent et al. 2002), and differences between the photometric systems (S-correction; Stritzinger et al. 2002) using the cross-filter K-corrections defined by Kim et al. (1996). The procedures are described in detail by Nugent et al. (2002), Hsiao et al. (2007), and de Jaeger et al. (2017). Note that this correction will be hereafter referred to as the AKS correction.

2.2 Subaru/HSC

To extend the Hubble diagram beyond $z = 0.3$, we use data from the HSC installed at the prime focus of the 8.2 m Subaru telescope, and the Low Resolution Imaging Spectrometer (LRIS; Oke et al. 1995, Rockosi et al. 2010) on the Keck-I 10 m telescope, both located at the Mauna Kea Observatory. HSC is a new instrument with the currently highest etendue, a combination of field of view (1.5° in diameter) and telescope size (8.2 m). The HSC transient survey started in November 2016 and had guaranteed access to 5–7 nights per month (dark phase) during six months. For each run, the COSMOS field (Capak et al. 2007) is observed about twice in each filter (*grizy*). The data are reduced with HSCPIPE (Bosch et al. 2017), a version of the LSST stack (Ivezić et al. 2009; Axelrod et al. 2010; Jurić et al. 2015). HSC astrometry and photometry are calibrated relative to the Pan-STARRS 1 (PS1) 3π catalog (Schlafly, Finkbeiner, Jurić et al. 2012; Tonry, Stubbs, Lykke, et al. 2012; Magnier et al. 2013). Final photometric points are obtained via point-spread-function photometry in the template-substracted images. We refer the reader to Aihara et al. (2017) for more

Table 1. Host-galaxy and SN parameters.

Parameters	Values	Refs
Host galaxy:		This work
Name	Anonymous	–
Type	Unknown	–
RA (J2000)	$\alpha = 09^{\mathrm{h}}58^{\mathrm{m}}53^{\mathrm{s}}\!.485$	–
Dec (J2000)	$\delta = +02°01'28''\!.62$	–
Heliocentric redshift	$z_{\mathrm{hel}} = 0.3398 \pm 0.0002$	–
Supernova:		This work
Name	SN 2016jhj	–
Type	SN II	–
RA (J2000)	$\alpha = 09^{\mathrm{h}}58^{\mathrm{m}}53^{\mathrm{s}}\!.505$	–
Dec (J2000)	$\delta = +02°01'28''\!.45$	–
Explosion date (JD)	2,457,719.6 ±2	–
Milky Way extinction (mag)	$E(B - V) = 0.0515$	(1)
Distance modulus (mag)	$\mu = 41.07 \pm 0.12^2 \pm 0.27^3$	–

Note: (1) Schlafly & Finkbeiner (2011); (2) uncertainty accounted for measurement errors of SN 2016jhj (velocity, magnitude, colour, redshift) of SN 2016jhj; (3) observed dispersion from the SN II Hubble diagram (σ_{obs}).

detailed information regarding photometric reduction and Yasuda et al. (in prep.) for details of the COSMOS transient survey.

When a SN candidate is detected, a photometric selection is performed based on two criteria specific to SNe II: a rapid light-curve rise (González-Gaitán et al. 2015) and a plateau resulting from the balance between cooling and recombination in the ejecta (Grassberg et al. 1971). In Figure 1, the *grizy* light curves of SN 2016jhj are displayed and the photometry is given in Table 2. As Figure 1 shows, the first SN II criterion is satisfied with a fast light-curve rise time in the z band of ~ 5 days. The second SN II criterion is also fulfilled with the presence of a clear plateau in the *rizy* light curves at an apparent magnitude of ~ 23 mag for more than 50 days. To estimate the explosion date we use the i band, for which the first photometric point (JD 2,457,721.55; Nov. 29, 2016; UT dates are used throughout this paper) was obtained four days after nondetection (JD 2,457,717.62; Nov. 25, 2016). In this paper, the explosion date is chosen as the median value between these two epochs and thus is estimated to be JD 2,457,719.56 ± 2. It is worth noting the quality of the light curve obtained using the HSC relative to one recent high-redshift SN II (PS1-13bni; Gall et al. 2017) observed by the Panoramic Survey Telescope & Rapid Response System 1 (Pan-STARRS1; Kaiser et al. 2010).

From this first HSC run, SN 2016jhj was our best high-redshift SN II candidate, with an estimated host-galaxy photometric redshift of ~ 0.33. Details of the host-galaxy and SN 2016jhj are listed in Table 1. As a proof of concept to demonstrate that we are now able to attempt high-redshift SN II cosmology ($z \gtrsim 0.3$), we obtained an optical spectrum using LRIS on the Keck-I telescope on 2017 January 3 (JD 2,457,756; 29.40 days after the explosion in the rest frame), with a total exposure time of one hour. LRIS is equipped with an atmospheric dispersion corrector, so the correct continuum shape is obtained. The reduction and the calibration were performed following standard procedures (bias subtraction, flat-field correction, one-dimensional extraction, wavelength and flux calibration) described by Silverman et al. (2012). In Figure 2, the observed spectrum (in black) to-

Table 2. SN 2016jhj *grizy* fluxes and magnitudes, and 1σ uncertainties.

JD – 2,400,000	Filters	flux (err)	mag (err)
57717.57	HSC-*g*	0.056 (0.560)	30.134 (10.908)
57755.61	HSC-*g*	27.298 (0.208)	23.410 (0.008)
57778.45	HSC-*g*	8.077 (0.241)	24.732 (0.032)
57785.39	HSC-*g*	5.738 (0.211)	25.103 (0.040)
57807.37	HSC-*g*	0.983 (0.215)	27.018 (0.238)
57834.32	HSC-*g*	0.370 (0.193)	28.080 (0.568)
57841.29	HSC-*g*	0.428 (0.202)	27.921 (0.513)
57869.33	HSC-*g*	0.269 (0.265)	28.425 (1.068)
57720.60	HSC-*r*2	62.929 (0.251)	22.503 (0.004)
57747.53	HSC-*r*2	64.971 (0.353)	22.468 (0.006)
57776.42	HSC-*r*2	29.365 (0.280)	23.330 (0.010)
57786.45	HSC-*r*2	23.778 (0.218)	23.560 (0.010)
57807.48	HSC-*r*2	11.595 (0.282)	24.339 (0.026)
57818.52	HSC-*r*2	5.289 (0.274)	25.191 (0.056)
57837.26	HSC-*r*2	1.938 (0.292)	26.282 (0.164)
57844.33	HSC-*r*2	2.441 (0.245)	26.031 (0.109)
57866.25	HSC-*r*2	1.767 (0.327)	26.382 (0.201)
57717.62	HSC-*i*2	-0.577 (0.352)	0.000 (0.000)
57721.55	HSC-*i*2	58.780 (0.432)	22.577 (0.008)
57747.62	HSC-*i*2	69.314 (0.404)	22.398 (0.006)
57755.51	HSC-*i*2	53.383 (0.290)	22.681 (0.006)
57776.54	HSC-*i*2	38.952 (0.279)	23.024 (0.008)
57783.43	HSC-*i*2	36.641 (0.361)	23.090 (0.011)
57786.58	HSC-*i*2	35.821 (0.521)	23.115 (0.016)
57809.42	HSC-*i*2	22.269 (0.472)	23.631 (0.023)
57816.47	HSC-*i*2	13.340 (0.262)	24.187 (0.021)
57835.26	HSC-*i*2	5.563 (0.427)	25.137 (0.083)
57842.27	HSC-*i*2	5.437 (0.426)	25.162 (0.085)
57869.27	HSC-*i*2	3.707 (0.543)	25.578 (0.159)
57870.35	HSC-*i*2	5.769 (0.628)	25.097 (0.118)
57715.55	HSC-*z*	0.182 (0.566)	28.849 (3.372)
57721.60	HSC-*z*	51.651 (0.621)	22.717 (0.013)
57745.57	HSC-*z*	77.277 (0.637)	22.280 (0.009)
57755.45	HSC-*z*	66.068 (0.610)	22.450 (0.010)
57774.50	HSC-*z*	57.847 (0.255)	22.594 (0.005)
57779.52	HSC-*z*	59.008 (2.391)	22.573 (0.044)
57783.55	HSC-*z*	56.668 (0.449)	22.617 (0.009)
57805.37	HSC-*z*	45.425 (0.571)	22.857 (0.014)
57816.31	HSC-*z*	28.646 (0.491)	23.357 (0.019)
57834.44	HSC-*z*	18.206 (0.457)	23.849 (0.027)
57841.41	HSC-*z*	18.320 (0.582)	23.843 (0.034)
57866.36	HSC-*z*	13.589 (0.887)	24.167 (0.071)
57872.26	HSC-*z*	13.230 (0.740)	24.196 (0.061)
57924.28	HSC-*z*	5.033 (2.587)	25.246 (0.558)
57715.62	HSC-*y*	-0.732 (0.771)	0.000 (0.000)
57748.53	HSC-*y*	81.048 (7.328)	22.228 (0.098)
57757.52	HSC-*y*	55.130 (1.238)	22.647 (0.024)
57778.62	HSC-*y*	42.227 (2.034)	22.936 (0.052)
57787.47	HSC-*y*	36.858 (0.880)	23.084 (0.026)
57811.40	HSC-*y*	24.922 (1.364)	23.509 (0.059)
57819.47	HSC-*y*	14.463 (0.751)	24.099 (0.056)
57833.38	HSC-*y*	8.264 (1.115)	24.707 (0.147)
57837.49	HSC-*y*	16.558 (10.402)	23.952 (0.682)
57842.34	HSC-*y*	8.474 (1.266)	24.680 (0.162)
57863.28	HSC-*y*	8.128 (1.571)	24.725 (0.210)
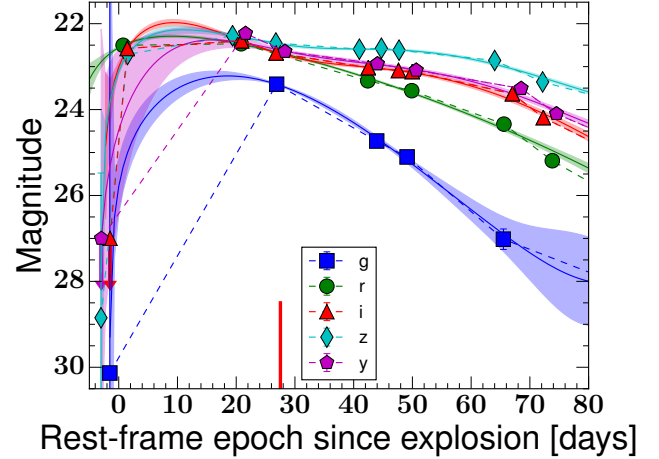
Figure 1. SN 2016jhj *grizy* light curves from the Hyper Suprime-Cam on the 8.2 m Subaru telescope. The blue squares, green circles, red triangles, cyan diamonds, and magenta pentagons are (respectively) the *g*, *r*, *i*, *z*, and *y* light curves. The vertical red line represents the epoch of the visual-wavelength spectrum since the explosion. For each filter, the solid curve is the best fit from the Gaussian-process interpolation described in Section 3.2. The filled region represents the 1σ uncertainty of the regression curve. The dashed lines are shown only to guide the eye. The assumed explosion date is JD 2,457,716.6 ± 1.0.

gether with the best SN spectral library match found (in red) by the Supernova Identification code (SNID; Blondin & Tonry 2007) are shown. The best match corresponds to the Type II SN 2004et (Sahu et al. 2006), which confirms the nature of our transient. Note that among all matches found by SNID (70), more than 85% were SNe II and around 15% SNe IIb (e.g., SN 1993J; Filippenko et al. 1993). However, it is worth noting that SNe IIb can be clearly excluded based on the observed light curve.

The heliocentric redshift used in this work was derived directly from the SN spectrum using the superimposed host-galaxy emission lines. In the spectrum, we are able to identify three features: [O II] λ3727.3, [O III] λ5006.8, and Hα λ6562.81, for which we respectively obtain very consistent redshifts of 0.3397±0.0001, 0.3399±0.0002, and 0.3400±0.0001 (note also the possible presence of the [S II] λ6717 emission line at the same redshift).In Figure 2, the emission lines used to derive the redshift are highlighted in blue. The final heliocentric redshift value is taken as 0.3398 ± 0.0002 (weighted average). Finally, owing to a lack of telescope time, we were able to observe only one candidate, even though the HSC survey provided us with additional SN II candidates.

3   METHODOLOGY

We now describe how we derive the Hubble diagram, and in particular how the expansion velocities, magnitudes, and colours are estimated. In this paper, the methodology and SN 2016jhj are the main differences with de Jaeger et al. (2017).
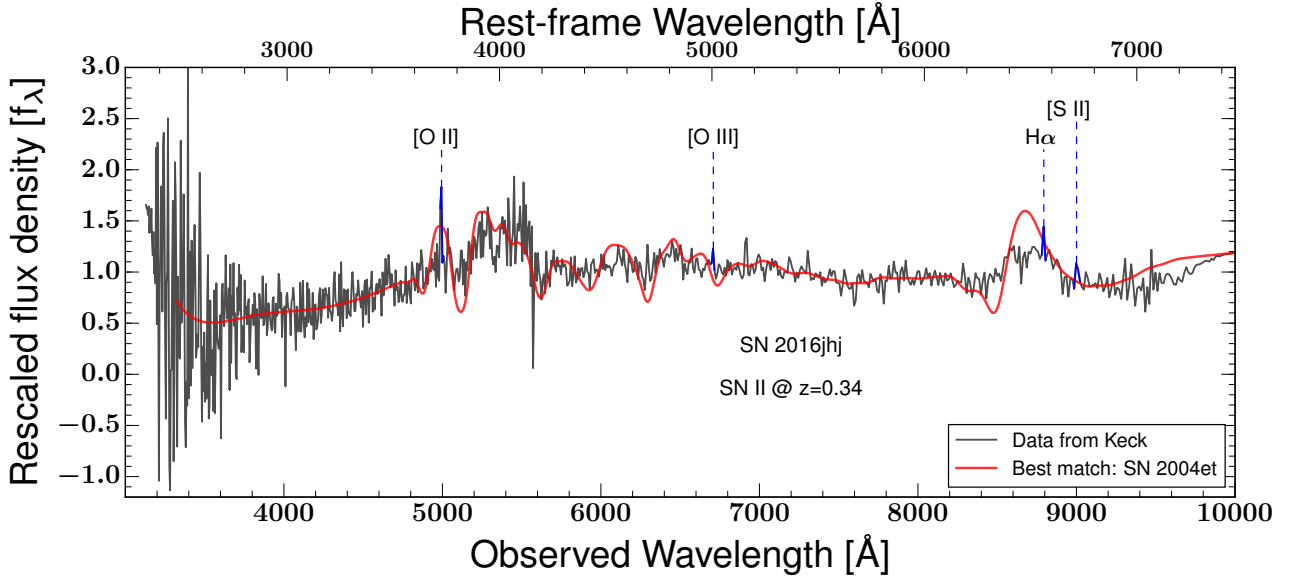
Figure 2. SN 2016jhj visual-wavelength spectrum obtained with LRIS on the Keck-I telescope. The SN 2016jhj spectrum (in black) is compared to a SN spectral library (in red) using SNID. The best fit is SN 2004et, a SN II. Note that the spectrum is binned on a logarithmic wavelength axis (Blondin & Tonry 2007) and the redshift written was derived from the narrow host-galaxy emission lines. Four emission lines from the host galaxy are also highlighted in blue: [O II] $\lambda3727.3$, [O III] $\lambda5006.8$, Hα $\lambda6562.81$, and [S II] $\lambda6717.67$.

3.1 Expansion velocities

To apply the SCM, it is fundamental to measure the expansion velocity of the ejecta. Generally, the velocity is estimated from the minimum flux of the absorption component of the P-Cygni profile of an optically thin line formed by pure scattering, such as Fe II $\lambda5018$. However, for noisy spectra and at early epochs, the Fe II features are often buried in the noise, making them unsuitable for velocity measurement. Even though it is less associated with the photospheric velocity, more recently the Hβ $\lambda4861$ absorption line has been proposed (Nugent et al. 2006; Poznanski et al. 2010; Takáts & Vinkó 2012; de Jaeger et al. 2017) as a velocity proxy. This line has the advantage of being stronger than Fe II $\lambda5018$, and thus easier to measure. Note that a linear relation was derived between the Hβ and Fe II velocities (Poznanski et al. 2010; Takáts & Vinkó 2012; de Jaeger et al. 2017), with a dispersion equivalent to an additional uncertainty of about 200–400 km s^{-1}.

However, at high redshift, spectra are so noisy that even the Hβ $\lambda4861$ absorption is not clearly visible; hence, some authors attempt to use other methods. In this section, we describe the cross-correlation technique developed by Poznanski et al. (2009).

In this method, the Hβ $\lambda4861$ velocity is determined by computing the cross-correlation (using the Tonry & Davis 1979 algorithm) between the observed spectra and a library of SNe II using SNID for which the Hβ $\lambda4861$ velocities can be measured precisely. This method has several advantages such as its simplicity, its robustness, and its utility for broad and noisy lines.

We used templates of six SNe II from the original SNID library together with a new set of spectral templates (Gutiérrez et al., in prep.). This new library consists of SNe II with well-constrained explosion epochs from the CSP-I and the Carnegie Type II Supernova Survey
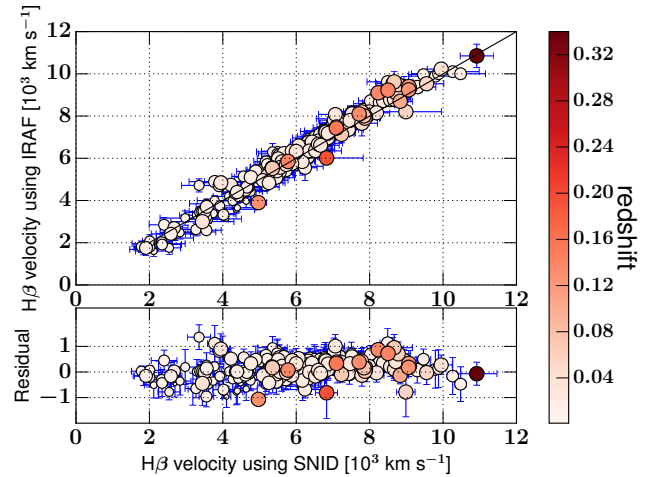

Figure 3. Comparison between the Hβ $\lambda4861$ velocities measured from the cross-correlation method with SNID and those determined from the absorption minima of Hβ $\lambda4861$ using IRAF. The residuals are plotted in the bottom panel. The black line represents a slope of unity. The colour bar on the right side represents the different redshifts. The marker size increases with redshift in order to highlight the high-redshift spectra — those typically with more noise. Note that the brown point at top right corresponds to SN 2016jhj, our distant SN II.

(Galbany et al. 2016). Briefly, we cross-correlated each observed spectrum only to the SN II library, constraining the wavelength range to 4400–6000Å (rest frame) in order to avoid the Hα $\lambda6563$ line. As the redshift is known, we use the "forcez" option available in SNID to directly run a set of correlations, with the input and template spectra trimmed to match at this redshift. For each spectrum, the resulting

velocities are the sum of the template velocities and the relative Doppler shift between the observed spectrum and the template. Finally, we select only the velocities of the best-fitting templates (top 10% of *rlap*[5] values) and calculate a weighted velocity mean. Note also that the spectrum epoch is not used as an input parameter because SNe II evolve at different speeds; we employ only the observed spectra with epochs between 15 and 90 days post-explosion, during the photospheric phase. In order to test this method, for each spectrum the Hβ λ4861 velocity is also estimated through the minimum flux of the absorption component of the P-Cygni profile using IRAF[6]. In Figure 3, the Hβ λ4861 velocities measured from both methods are compared. As we can see, the velocities derived from the minimum flux of the Hβ λ4861 absorption line and those estimated using SNID are correlated with a dispersion of $\sim$ 400 km s^{-1}. The correlation is also good for the high-z SN II spectra with a lower signal-to-noise ratio (S/N). This exercise validates the use of the cross-correlation method presented by Poznanski et al. (2009) and shows its importance for the high-z spectrum velocity measurement. However, it is worth remarking that the cross-correlation method introduces a bias, as we clearly see a trend in the residuals (Pearson factor of $\sim$ 0.35). As already mentioned by D'Andrea et al. (2010) and Takáts & Vinkó (2012), this bias is caused by the template selection, and it is more important at early and late epochs. Note also that SN 2016jhj has the highest velocity among the the sample, merely due to a Malmquist bias: as the HSC survey searches for the highest-redshift SNe, they then to find only very luminous objects.

After computing the Hβ λ4861 velocity for each SN at all available epochs, we do an interpolation/extrapolation using a power law of the form (Hamuy 2001)

$$v(t) = At^\gamma, \tag{1}$$

where A and γ are two free parameters obtained by least-squares minimisation for each individual SN and t is the rest-frame epoch from the explosion. Following the work done by de Jaeger et al. (2017), a Monte Carlo simulation is performed to obtain the velocity uncertainty. We also add to this error a value of 150 km s^{-1}, in quadrature, to account for unknown host-galaxy peculiar velocities. When a SN has only one spectrum available, the free parameter γ is fixed to a value of -0.407 ± 0.173, which corresponds to the median value derived from the CSP sample (de Jaeger et al. 2017). Note the difference between the methodology used by Gall et al. (2017) and in this work: Gall et al. (2017) measured the Hβ λ4861 velocity using IRAF, which could be very difficult for very high-redshift SNe II and their noisy spectra. Additionally, to derive the velocity at 50 days post-explosion, they assumed the same power law for each SN, while in our work, we derive a specific power law for each SN having at least two spectra.

---

[5] The *rlap* parameter is akin to a quality parameter: the higher the *rlap*, the better the correlation (Blondin & Tonry 2007).
[6] IRAF is distributed by the National Optical Astronomy Observatory, which is operated by the Association of Universities for Research in Astronomy (AURA) under cooperative agreement with the US National Science Foundation (NSF).
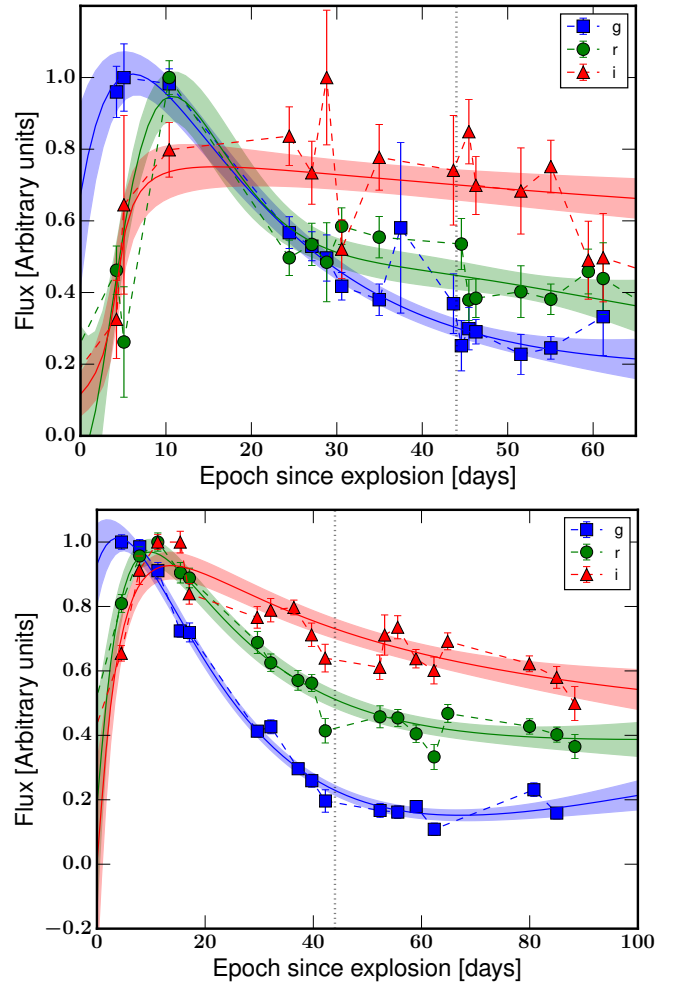

Figure 4. *Top:* SN 2007nr AKS-corrected light curves in flux. The explosion date and heliocentric redshift are (respectively) JD 2,454,542.9 $\pm$ 6.0 and z = 0.14. *Bottom:* SN 05D4dn AKS-corrected light curves in flux. The explosion date and heliocentric redshift are JD 2,454,742.7 $\pm$ 9.0 and z = 0.19, respectively. For both SNe, the *gri* bands are shown in blue, red, and green (respectively). For each filter, the solid curve is the best fit from the Gaussian-process regression. The filled region represents the 1σ uncertainty of the regression curve. The dotted black line represents the epoch 44 days after the explosion in order to compare between the linear and the Gaussian-process interpolation.

3.2 Light-curve interpolation

We model the SN light curves using the hierarchical Gaussian processes (also known as Bayesian smoothing splines) to interpolate the magnitudes and colours at different epochs. This technique has the advantage over other methods of allowing the inclusion of uncertainty information, thus producing less-biased interpolated values. Additionally, this method is very powerful for SN light curves having incomplete or noisy photometric data (Mandel et al. 2009, 2011; Burns et al. 2014; Lochner et al. 2016).

For this purpose, we use the fast and flexible Python library GEORGE developed by Ambikasaran et al. (2014). In Figure 4, two examples of incomplete and noisy SN light-curve fits are shown. These two SNe (SN 2007nr and
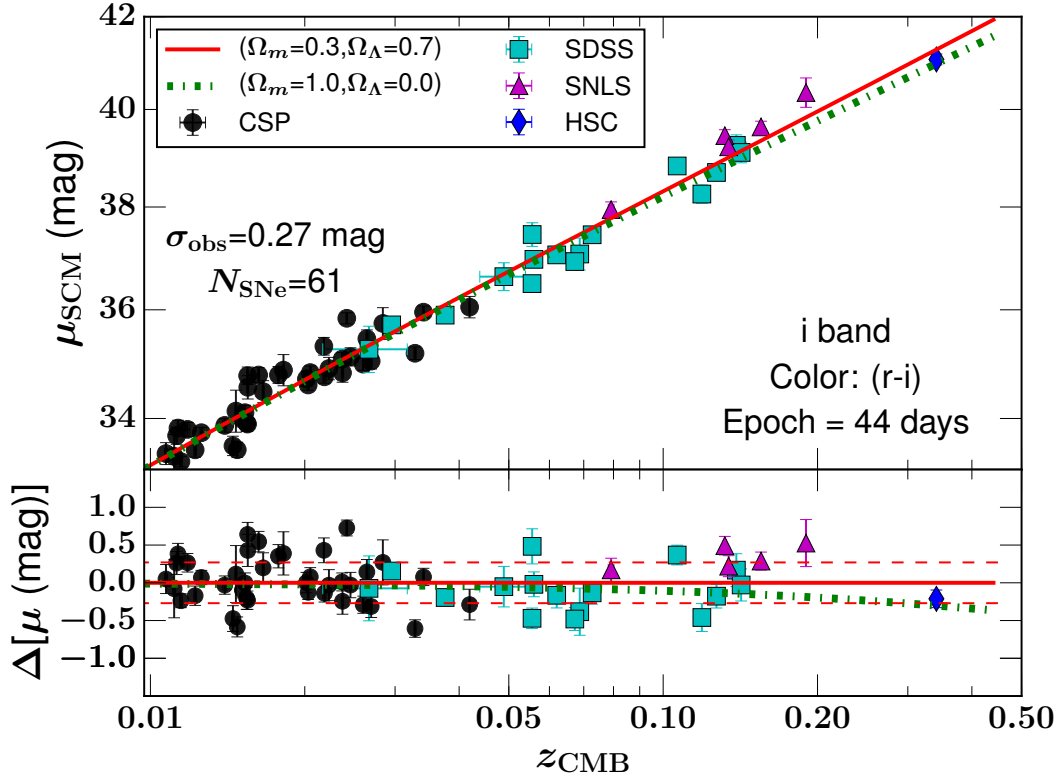
Figure 5. Hubble diagram (top) and residuals from the ΛCDM model (bottom) using the SCM as applied to the data taken from CSP-I (black circles; de Jaeger et al. 2017), SDSS (cyan squares; D'Andrea et al. 2010), SNLS (magenta triangles; de Jaeger et al. 2017), and HSC (blue diamond; this work). The red solid line is the Hubble diagram for the ΛCDM model ($\Omega_m = 0.3$, $\Omega_\Lambda = 0.7$), while the green dash-dot line is for an Einstein-de Sitter cosmological model ($\Omega_m = 1.0$, $\Omega_\Lambda = 0.0$). In both models, we assume a Hubble constant of 70 km s^{-1} Mpc^{-1}. We also present the number of SNe II available at this epoch (N_{SNe}), the epoch after the explosion, and the observed dispersion (σ_{obs}).

SN 05D4dn) are from the SDSS and SNLS samples, respectively. As shown in the figure, the best fit from the Gaussian process is very satisfactory during the plateau phase and allows us to derive the magnitudes and colours. Note that this procedure differs from that of de Jaeger et al. (2017), who did a simple linear interpolation. In this figure, we also clearly see the differences between the magnitudes derived using a linear or a Gaussian interpolation. For instance, for SN 2007nr at epoch 44 days after the explosion, the difference between the two methods in the *r*-band is ∼ 0.2 mag. In addition to SN 2007nr and SN 05D4dn, five other SNe show differences in the *r* or *i* bands larger than 0.1 mag: SN 18321, SN 2007kz, SN 2007nv, SN 2007nw, and SN 2007ny (all from the SDSS). Finally, it is important to note that in this work, we never extrapolate the magnitude.

3.3 Hubble diagram

In the SCM, we use two corrections to standardise the SN observed magnitude: the expansion velocity, and the colour correction that accounts for host-galaxy extinction. Thus,

the observed magnitude can be modeled as

$$m_i^{\mathrm{model}} = \mathcal{M}_i - \alpha \log_{10}\left(\frac{v_{\mathrm{H}\beta}}{< v_{\mathrm{H}\beta} > \mathrm{\ km\ s^{-1}}}\right) \\ + \beta(r-i) + 5\log_{10}(\mathcal{D}_L(z_{\mathrm{CMB}}|\Omega_{\mathrm{m}}, \Omega_\Lambda)), \quad (2)$$

where $(r-i)$ is the colour, $\mathcal{D}_L(z_{\mathrm{CMB}}|\Omega_{\mathrm{m}}, \Omega_\Lambda)$ is the luminosity distance ($\mathcal{D}_L = \mathrm{H}_0 d_L$) for a cosmological model depending on the cosmological parameters Ω_m, Ω_Λ, the CMB redshift z_{CMB}, and the Hubble constant. Finally, α, β, and $\mathcal{M}_i$ are also free parameters, with $\mathcal{M}_i$ corresponding to the "Hubble-constant-free" absolute magnitude ($\mathcal{M}_i = \mathrm{M}_i - 5 \log_{10}(\mathrm{H}_0) + 25$). Note that we center the velocity and colour ($(r-i)- < (r-i) >$) distributions using the mean velocity ($< v_{H\beta} > \approx 5910$ km s^{-1}) and the mean colour ($< (r-i) > \approx -0.02$ mag) of the whole sample, respectively.

To derive the Hubble diagram and to determine the best-fit parameters, as done by Poznanski et al. (2009), D'Andrea et al. (2010), and de Jaeger et al. (2017), a Monte Carlo Markov Chain (MCMC) simulation is performed. In particular, here we use the Python package EMCEE developed by Foreman-Mackey et al. (2013), and we minimise the likelihood function defined as

$$-2\ln(\mathcal{L}) = \sum_{\mathrm{SN}}\left\{\frac{[m_i^{\mathrm{obs}} - m_i^{\mathrm{model}}]^2}{\sigma_{\mathrm{tot}}^2} + \ln(\sigma_{\mathrm{tot}}^2)\right\}, \quad (3)$$
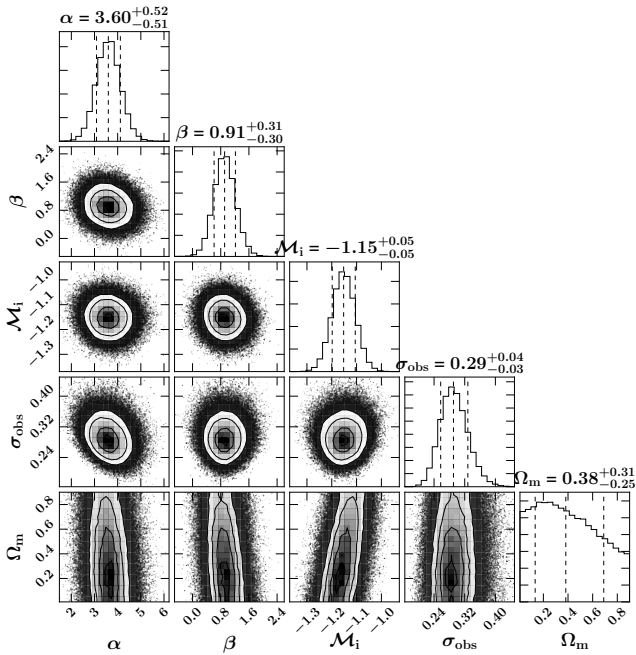
Figure 6. Corner plot showing all of the one- and two-dimensional projections. Contours are shown at 1σ, 2σ, and 3σ. The five free parameters are plotted: α, β, $\mathcal{M}_{\lambda 1}$, $\sigma_{\rm obs}$, and Ω_m. To make this figure we use the corner plot package (triangle.py v0.1.1. Zenodo. 10.5281/zenodo.11020). In deriving this figure, we assume a flat universe.

where we sum over all SNe II available for one specific epoch, $m_i^{\rm obs}$ is the observed magnitude corrected for AKS, $m_i^{\rm model}$ is the model defined in Equation 2, and the total uncertainty $\sigma_{\rm tot}$ (corresponding to the error propagation of the model) is defined as

$$\sigma_{\rm tot}^2 = \sigma_{m_i}^2 + \left(\frac{\alpha}{\ln 10}\frac{\sigma_{v_{\rm H\beta}}}{v_{\rm H\beta}}\right)^2 + (\beta\sigma_{(r-i)})^2$$
$$+ \left(\sigma_z \frac{5(1+z)}{z(1+z/2)\ln(10)}\right)^2 + \sigma_{\rm obs}^2. \tag{4}$$

Note that to measure the deviations between the observed SNe and the model, a term ($\sigma_{\rm obs}$) is added to the total error. This value includes true intrinsic scatter in the Hubble diagram (minimum uncertainty in any distance determination using the SCM) and any misestimates of the photometric, velocity, or redshift uncertainties. This term is also known as $\sigma_{\rm sys}$ (Poznanski et al. 2009) or $\sigma_{\rm int}$ (e.g., Conley et al. 2011; de Jaeger et al. 2017).

4 RESULTS

In this results section, we will first attempt to extend the low-redshift Hubble diagram to higher redshifts, and then constrain the cosmological parameters.

4.1 Fixed cosmology

We use the complete SN II sample, consisting of slowly declining (SNe IIP) and rapidly declining (SNe IIL) objects, as

de Jaeger et al. (2015) demonstrated that the Hubble residual does not depend on the slope of the plateau. This was also recently confirmed by Gall et al. (2017). Our sample available at epoch 44 days after the explosion consists of 60 SNe II (39[7], 16, and 5 SNe II from CSP, SDSS, and SNLS, respectively) together with the high-z SN 2016jhj from HSC. The relevant information for all SNe II in this sample is given in Appendix A, Table A1. Note that the majority of the distance moduli are consistent with those of de Jaeger et al. (2017), but seven SNe II (one CSP-I, four SDSS, and two SNLS) are not, because of differences in velocities (the cross-correlation method shows some bias for the extreme epochs; see 3.1) or in magnitudes/colours (some of these SNe II have very noisy light curves, and were only linearly interpolated by de Jaeger et al. (2017)).

First, we try to construct a high-z Hubble diagram by finding the best-fit values (α, β, $\mathcal{M}_i$, and $\sigma_{\rm obs}$) using a flat Universe ($\Omega_m + \Omega_\Lambda = 1$, $\Omega_m = 0.3$) assumption. We find $\alpha = 3.57^{+0.52}_{-0.50}$, $\beta = 0.95^{+0.29}_{-0.29}$, and $\mathcal{M}_i = -1.16^{+0.04}_{-0.04}$, with an observed dispersion $\sigma_{\rm obs} = 0.27$ mag. In Figure 5, the Hubble diagram and the Hubble residuals of the combined data are displayed. Note that to derive the best epoch to use, the minimisation of dispersion in the Hubble diagram is our figure of merit. The best epoch is found to be 44 days after the explosion during the plateau phase. This epoch is similar to the 50 days in the rest frame (post-explosion) used by other SN II cosmology studies (Nugent et al. 2006; Poznanski et al. 2009; Olivares E. et al. 2010; D'Andrea et al. 2010).

The observed dispersion found is consistent with the results from previous studies (0.26 mag, Nugent et al. 2006; 0.25 mag, Poznanski et al. 2010; 0.29 mag, D'Andrea et al. 2010; and 0.27 mag, de Jaeger et al. 2017) and corresponds to 12–13% in distance. Note that without any correction, the observed dispersion is more than twice as large (0.60 mag; $\sim 27\%$ in distance). The best-fit parameters are nearly identical to those of de Jaeger et al. (2017), except for α, which is slightly different ($\alpha = 3.57^{+0.52}_{-0.50}$ versus $\alpha = 3.18^{+0.41}_{-0.41}$). The discrepancy in α is easily explained by the difference of methodology used to derive the velocities. de Jaeger et al. (2017) performed the minimum absorption technique, while in this work we use the cross-correlation method. If the cross-correlation method is applied only to the de Jaeger et al. (2017) sample (without SN 2016jhj), we derive a value of α identical to that derived with the whole sample.

4.2 Ω_m derivation

As demonstrated in Section 4.1, we are able to construct a high-z Hubble diagram in which the differences between the expansion histories start to be distinguishable. Thus, as performed by de Jaeger et al. (2017), we try to put some constraints on the cosmological parameters. For this purpose, we assume a flat universe ($\Omega_m + \Omega_\Lambda = 1$), a Hubble constant $H_0 = 70$ km s^{-1} Mpc^{-1}, and leave Ω_m as a free parameter together with α, β, $\mathcal{M}_i$, and $\sigma_{\rm obs}$. All of the best-fit parameters (α, β, $\mathcal{M}_i$, and $\sigma_{\rm obs}$) are shown in Figure 6,

---

[7] With respect to de Jaeger et al. (2017), SN 2005es and SN 2008F are not used owing to the lack of a spectrum at epochs later than 15 days (our cut for the cross-correlation method), while SN 2006ms is available at epoch 44 days after the explosion.

where a corner plot with all of the one- and two-dimensional projections is displayed. Note that all the parameters are slightly different from those obtained for a fixed cosmology (ΛCDM cosmological model) because here Ω_m is left as a free parameter.

A value for the matter density of $\Omega_m = 0.38^{+0.31}_{-0.25}$ is derived, which gives a density of dark energy of $\Omega_\Lambda = 0.62^{+0.25}_{-0.31}$. Our prior probability distribution is defined to have uniform probability for $0.01 \leq \Omega_m \leq 0.9$, as well as α, β, $\mathcal{M}_{\lambda1} \neq 0$. Note that if we choose a more restrictive prior for Ω_m, such as $0.2 \leq \Omega_m \leq 0.6$, the uncertainties decrease and we derive a value of $\Omega_m = 0.38^{+0.14}_{-0.13}$. On the other hand, if we take less restrictive limits ($0.01 \leq \Omega_m \leq 2.5$,), the values and the uncertainties are not much larger ($\Omega_m = 0.50^{+0.56}_{-0.34}$).

The value derived in this work is consistent with that obtained by de Jaeger et al. (2017) ($\Omega_m = 0.41^{+0.31}_{-0.27}$) and confirms the evidence for dark energy using SNe II. While the uncertainties we obtain here are far from the precision achieved using SNe Ia (e.g., Betoule et al. 2014), this work confirms the great potential of SNe II as distance indicators and our capacity to extend the current Hubble diagrams beyond $z = 0.3$. Nevertheless, this work addresses the necessity of dedicating more observing time to high-redshift SNe II in order to improve their utility as independent distance indicators and make them comparable in precision to SNe Ia.

5 CONCLUSIONS

In this paper, we demonstrate that we are able to apply the SCM and extend the SN II Hubble diagram beyond $z = 0.3$. Although SNe II are not currently competitive with SNe Ia in terms of dispersion (~ 0.27 mag vs. ~ 0.10 mag) or sample size (~ 61 SNe II vs. ~ 740 SNe Ia), this work is comparable to the early SN Ia results (Perlmutter et al. 1997), showing that SNe II are a useful complementary and independent method for constraining the nature of dark energy. We summarise our results as follows.

(i) We test the cross-correlation method proposed by Poznanski et al. (2009) at high redshift and confirm its potential. This will be an asset for low-S/N spectra.

(ii) We obtain a dispersion of 0.27 mag using the SCM and 61 SNe II at a redshift up to ~ 0.34, which is most distant SN II Hubble diagram ever built using the SCM.

(iii) This high-z Hubble diagram confirmed the result found in the literature in terms of dispersion or best-fit parameters (α, β, $\mathcal{M}_i$).

(iv) We derived cosmological parameters (Ω_m) consistent with ΛCDM: $\Omega_m = 0.38^{+0.31}_{-0.25}$. The uncertainties are somewhat better than those in previous studies of SN II cosmology.

the University of California, and NASA; the observatory was made possible by the generous financial support of the W.M. Keck Foundation. This work is based in part on data produced at the Canadian Astronomy Data Centre as part of the CFHT Legacy Survey, a collaborative project of the National Research Council of Canada and the French Centre National de la Recherche Scientifique. The work is also based on observations obtained at the Gemini Observatory, which is operated by the Association of Universities for Research in Astronomy, Inc., under a cooperative agreement with the NSF on behalf of the Gemini partnership: the NSF, the STFC (United Kingdom), the National Research Council (Canada), CONICYT (Chile), the Australian Research Council (Australia), CNPq (Brazil) and CONICET (Argentina). This research used observations from Gemini program number: GN-2005A-Q-11, GN-2005B-Q-7, GN-2006A-Q-7, GS-2005A-Q-11 and GS-2005B-Q-6, and GS-2008B-Q-56. This research has made use of the NASA/IPAC Extragalactic Database (NED), which is operated by the Jet Propulsion Laboratory, California Institute of Technology, under contract with NASA and of data provided by the Central Bureau for Astronomical Telegrams.

REFERENCES

Aihara H., Armstrong R., Bickerton S., et al., 2017, preprint, (arXiv:1702.08449)

Ambikasaran S., Foreman-Mackey D., Greengard L., Hogg D. W., O'Neil M., 2014, preprint, (arXiv:1403.6015)

Anderson J. P., González-Gaitán S., Hamuy M., et al., 2014, ApJ, 786, 67

Astier P., Guy J., Regnault N., et al., 2006, A&A, 447, 31

Axelrod T., Kantor J., Lupton R. H., Pierfederici F., 2010, in Software and Cyberinfrastructure for Astronomy. p. 774015, doi:10.1117/12.857297

Barbon R., Ciatti F., Rosino L., 1979, A&A, 72, 287

Bennett C. L., Hill R. S., Hinshaw G., et al., 2003, ApJS, 148, 1

Betoule M., Kessler R., Guy J., et al., 2014, A&A, 568, A22

Blake C., Glazebrook K., 2003, ApJ, 594, 665

Blondin S., Tonry J. L., 2007, ApJ, 666, 1024

Bosch J., Armstrong R., Bickerton S., et al., 2017, preprint, (arXiv:1705.06766)

Burns C. R., Stritzinger M., Phillips M. M., et al., 2014, ApJ, 789, 32

Capak P., Aussel H., Ajiki et al., 2007, ApJS, 172, 99

Cappellaro E., Botticella M. T., Pignata G., et al., 2015, A&A, 584, A62

Chevalier R. A., 1976, ApJ, 207, 872

Conley A., Guy J., Sullivan M., et al., 2011, ApJS, 192, 1

D'Andrea C. B., Sako M., Dilday B., et al., 2010, ApJ, 708, 661

de Jaeger T., González-Gaitán S., Anderson J. P., et al., 2015, ApJ, 815, 121

de Jaeger T., González-Gaitán S., Hamuy M., et al., 2017, ApJ, 835, 166

Falk S. W., Arnett W. D., 1977, ApJS, 33, 515

Filippenko A. V., 1997, ARA&A, 35, 309

Filippenko A. V., 2000, in Holt S. S., Zhang W. W., eds, American Institute of Physics Conference Series Vol. 522, 123 (arXiv:astro-ph/0002264), doi:10.1063/1.1291705

Filippenko A. V., Matheson T., Ho L. C., 1993, ApJ, 415, L103

Fixsen D. J., Cheng E. S., Gales J. M., et al., 1996, ApJ, 473, 576

Foreman-Mackey D., Hogg D. W., Lang D., Goodman J., 2013, PASP, 125, 306

Frieman J. A., Bassett B., Becker A., et al., 2008, AJ, 135, 338

Galbany L., Hamuy M., Phillips M. M., et al., 2016, AJ, 151, 33

Gall E. E. E., Kotak R., Leibundgut B., et al., 2017, preprint, (arXiv:1705.10806)

Gilmozzi R., Spyromilio J., 2007, The Messenger, 127

González-Gaitán S., Tominaga N., Molina J., et al., 2015, MNRAS, 451, 2212

Grassberg E. K., Imshennik V. S., Nadyozhin D. K., 1971, Ap&SS, 10, 28

Guy J., Sullivan M., Conley A., et al., 2010, A&A, 523, A7

Hamuy M. A., 2001, PhD thesis, The University of Arizona

Hamuy M., Folatelli G., Morrell N. I., et al., 2006, PASP, 118, 2

Hamuy M., Pinto P. A., 2002, ApJ, 566, L63

Hamuy M., Phillips M. M., Suntzeff N. B., et al., 1996, AJ, 112, 2391

Hamuy M., Phillips M. M., Wells L. A., Maza J., 1993, PASP, 105, 787

Hsiao E. Y., Conley A., Howell D. A., et al., 2007, ApJ, 663, 1187

Inserra C., Smartt S. J., 2014, ApJ, 796, 87

Ivezić Z., Tyson J. A., Axelrod T., et al., 2009, in American Astronomical Society Meeting Abstracts 213. p. 460.03

Jaffe A. H., Ade P. A., Balbi A., et al., 2001, Physical Review Letters, 86, 3475

Janka H.-T., Langanke K., Marek A., Martínez-Pinedo G., Müller B., 2007, Phys. Rep., 442, 38

Johns M., McCarthy P., Raybould K., et al., 2012, in Ground-based and Airborne Telescopes IV. p. 84441H, doi:10.1117/12.926716

Jurić M., Kantor J., Lim K., et al., 2015, preprint, (arXiv:1512.07914)

Kaiser N., Burgett W., Chambers K., et al., 2010, in Ground-based and Airborne Telescopes III. p. 77330E, doi:10.1117/12.859188

Kasen D., Woosley S. E., 2009, ApJ, 703, 2205

Kessler R., et al., 2009, ApJS, 185, 32

Kim A., Goobar A., Perlmutter S., 1996, PASP, 108, 190

Kirshner R. P., Kwan J., 1974, ApJ, 193, 27

Li W., Leaman J., Chornock R., et al., 2011, MNRAS, 412, 1441

Lochner M., McEwen J. D., Peiris H. V., Lahav O., Winter M. K., 2016, ApJS, 225, 31

Magnier E. A., Schlafly E., Finkbeiner D., et al., 2013, ApJS, 205, 20

Mandel K. S., Narayan G., Kirshner R. P., 2011, ApJ, 731, 120

Mandel K. S., Wood-Vasey W. M., Friedman A. S., Kirshner R. P., 2009, ApJ, 704, 629

Minkowski R., 1941, PASP, 53, 224

Miyazaki S., Komiyama Y., Nakaya H., et al., 2012, in Ground-based and Airborne Instrumentation for Astronomy IV. p. 84460Z, doi:10.1117/12.926844

Nugent P., Kim A., Perlmutter S., 2002, PASP, 114, 803

Nugent P., Sullivan M., Ellis R., et al., 2006, ApJ, 645, 841

Oke J. B., Cohen J. G., Carr M., et al., 1995, PASP, 107, 375

Oke J. B., Sandage A., 1968, ApJ, 154, 21

Olivares E. F., Hamuy M., Pignata G., et al., 2010, ApJ, 715, 833

Perlmutter S., Aldering G., Goldhaber G., et al., 1999, ApJ, 517, 565

Perlmutter S., Gabi S., Goldhaber G., et al., 1997, ApJ, 483, 565

Perrett K., Balam D., Sullivan M., et al., 2010, AJ, 140, 518

Phillips M. M., 1993, ApJ, 413, L105

Planck Collaboration Ade P. A. R., Aghanim N., et al., 2013, preprint, (arXiv:1303.5076)

Poznanski D., Butler N., Filippenko A. V., et al., 2009, ApJ, 694, 1067

Poznanski D., Nugent P. E., Filippenko A. V., 2010, ApJ, 721, 956

Richardson D., Jenkins III R. L., Wright J., Maddox L., 2014, AJ, 147, 118

Riess A. G., Filippenko A. V., Challis P., et al., 1998, AJ, 116, 1009

Riess A. G., Macri L. M., Hoffmann S. L., et al., 2016, ApJ, 826, 56

Riess A. G., Press W. H., Kirshner R. P., 1996, ApJ, 473, 88

Rockosi C., Stover R., Kibrick R., et al., 2010, in Ground-based and Airborne Instrumentation for Astronomy III. p. 77350R, doi:10.1117/12.856818

Rodríguez Ó., Clocchiatti A., Hamuy M., 2014, AJ, 148, 107

Rubin D., Hayden B., 2016, ApJ, 833, L30

Sahu D. K., Anupama G. C., Srividya S., Muneer S., 2006, MN-RAS, 372, 1315

Sanders G. H., 2013, Journal of Astrophysics and Astronomy, 34, 81

Sanders N. E., Soderberg A. M., Gezari S., et al., 2015, ApJ, 799, 208

Schlafly E. F., Finkbeiner D. P., 2011, ApJ, 737, 103

Schlafly E. F., Finkbeiner D. P., Jurić M., et al., 2012, ApJ, 756, 158

Schmidt B. P., Suntzeff N. B., Phillips M. M., et al., 1998, ApJ, 507, 46

Schuecker P., Böhringer H., Collins C. A., Guzzo L., 2003, A&A, 398, 867

Seo H.-J., Eisenstein D. J., 2003, ApJ, 598, 720

Silverman J. M., Foley R. J., Filippenko A. V., et al., 2012, MN-RAS, 425, 1789

Smartt S. J., Eldridge J. J., Crockett R. M., Maund J. R., 2009, MNRAS, 395, 1409

Spergel D. N., Bean R., Doré O., et al., 2007, ApJS, 170, 377

Stritzinger M., Hamuy M., Suntzeff N. B., et al., 2002, AJ, 124, 2100

Takáts K., Vinkó J., 2012, MNRAS, 419, 2783

Taylor M., Cinabro D., Dilday B., et al., 2014, ApJ, 792, 135

Tonry J., Davis M., 1979, AJ, 84, 1511

Tonry J. L., Stubbs C. W., Lykke K. R., et al., 2012, ApJ, 750, 99

Valenti S., Howell D. A., Stritzinger M. D., et al., 2016, MNRAS,

Van Dyk S. D., Li W., Filippenko A. V., 2003, PASP, 115, 1289

White S. D. M., Navarro J. F., Evrard A. E., Frenk C. S., 1993, Nature, 366, 429

Woosley S. E., Weaver T. A., 1995, ApJS, 101, 181

APPENDIX A:

In Table A1, the relevant information for all SNe II used in the Hubble diagram is displayed. The first column gives the SN name, followed (in Column 2) by its reddening due to dust in our Galaxy (Schlafly & Finkbeiner 2011). In Column 3, we list the host-galaxy velocity in the CMB frame using the CMB dipole model presented by Fixsen et al. (1996). The explosion epoch is given in Column 4. In Column 5, the magnitude in the i band at epoch 44 days post-explosion is listed, followed by the $r - i$ colour at the same epoch in Column 6. Column 7 gives the Hβ velocity at epoch 44 days. Finally, in Columns 8 and 9 we respectively present the distance modulus measured using SCM and the survey from which the SN II originates.

This paper has been typeset from a TEX/LATEX file prepared by the author.

Table A1. The supernova sample

SN	A_VG mag	z_{CMB} (err)	Explosion date MJD	m_i mag	$r - i$ mag	$v_{H\beta}$ km s^{-1}	μ_{SCM} mag	Campaign
SN04er	0.070	0.014 (0.0001)	53271.8 (4.0)	16.72 (0.01)	0.208 (0.016)	7504 (453)	33.88 (0.13)	CSP-I
SN05J	0.075	0.015 (0.0001)	53382.8 (7.0)	16.99 (0.01)	-0.031 (0.011)	6039 (273)	33.99 (0.10)	CSP-I
SN05K	0.108	0.028 (0.0001)	53369.8 (7.0)	18.81 (0.02)	-0.127 (0.023)	5517 (831)	35.75 (0.30)	CSP-I
SN05Z	0.076	0.020 (0.0001)	53396.7 (8.0)	17.46 (0.01)	0.087 (0.014)	7037 (288)	34.61 (0.09)	CSP-I
SN05an	0.262	0.012 (0.0001)	53426.7 (4.0)	16.74 (0.01)	-0.021 (0.012)	6321 (368)	33.81 (0.12)	CSP-I
SN05dk	0.134	0.015 (0.0001)	53599.5 (6.0)	16.77 (0.02)	-0.069 (0.027)	6488 (474)	33.92 (0.15)	CSP-I
SN05dt	0.079	0.025 (0.0001)	53605.6 (9.0)	18.55 (0.01)	0.043 (0.018)	4824 (404)	35.12 (0.17)	CSP-I
SN05dw	0.062	0.017 (0.0001)	53603.6 (9.0)	17.67 (0.01)	-0.001 (0.02)	5469 (537)	34.49 (0.20)	CSP-I
SN05dx	0.066	0.026 (0.0001)	53615.9 (7.0)	19.24 (0.05)	0.283 (0.059)	4382 (328)	35.45 (0.17)	CSP-I
SN05dz	0.223	0.018 (0.0001)	53619.5 (4.0)	17.92 (0.02)	0.003 (0.028)	5665 (442)	34.79 (0.16)	CSP-I
SN05lw	0.135	0.027 (0.0001)	53716.8 (5.0)	17.96 (0.02)	0.167 (0.024)	7037 (480)	35.05 (0.14)	CSP-I
SN05me	0.070	0.022 (0.0001)	53721.6 (6.0)	18.34 (0.01)	-0.059 (0.011)	5869 (482)	35.32 (0.17)	CSP-I
SN06Y	0.354	0.034 (0.0001)	53766.5 (4.0)	18.66 (0.03)	-0.137 (0.036)	6853 (348)	35.96 (0.11)	CSP-I
SN06ai	0.347	0.015 (0.0001)	53781.8 (5.0)	16.82 (0.02)	-0.077 (0.026)	6226 (333)	33.9 (0.12)	CSP-I
SN06bl	0.144	0.033 (0.0001)	53823.8 (6.0)	18.12 (0.01)	-0.064 (0.016)	6168 (341)	35.18 (0.12)	CSP-I
SN06ee	0.167	0.014 (0.0001)	53961.9 (4.0)	17.47 (0.02)	0.005 (0.025)	3418 (297)	33.50 (0.18)	CSP-I
SN06ms	0.095	0.015 (0.0001)	54034.0 (12.0)	17.75 (0.02)	0.004 (0.029)	4191 (835)	34.12 (0.39)	CSP-I
SN06qr	0.126	0.015 (0.0001)	54062.8 (7.0)	18.12 (0.01)	0.075 (0.014)	4535 (514)	34.56 (0.23)	CSP-I
SN07P	0.111	0.042 (0.0001)	54118.7 (3.0)	18.96 (0.02)	-0.110 (0.023)	6143 (585)	36.06 (0.19)	CSP-I
SN07U	0.145	0.026 (0.0001)	54134.6 (6.0)	17.73 (0.01)	-0.091 (0.019)	6863 (381)	34.99 (0.12)	CSP-I
SN07W	0.141	0.011 (0.0001)	54136.8 (7.0)	17.31 (0.01)	-0.014 (0.017)	3441 (345)	33.37 (0.20)	CSP-I
SN07ab	0.730	0.024 (0.0001)	54123.8 (6.0)	17.63 (0.02)	-0.062 (0.024)	7838 (449)	35.09 (0.12)	CSP-I
SN07hm	0.172	0.024 (0.0001)	54335.6 (6.0)	18.77 (0.01)	-0.074 (0.016)	6161 (313)	35.84 (0.11)	CSP-I
SN07il	0.129	0.021 (0.0001)	54349.8 (4.0)	17.8 (0.02)	-0.027 (0.022)	6168 (337)	34.83 (0.12)	CSP-I
SN07sq	0.567	0.016 (0.0001)	54421.8 (3.0)	17.84 (0.01)	0.369 (0.016)	7167 (476)	34.79 (0.14)	CSP-I
SN08W	0.267	0.020 (0.0001)	54485.8 (6.0)	17.91 (0.02)	0.053 (0.029)	5620 (347)	34.72 (0.13)	CSP-I
SN08ag	0.229	0.015 (0.0001)	54479.8 (6.0)	16.82 (0.01)	-0.033 (0.018)	4795 (318)	33.44 (0.14)	CSP-I
SN08aw	0.111	0.011 (0.0001)	54517.8 (10.0)	16.11 (0.01)	0.015 (0.016)	6704 (261)	33.24 (0.09)	CSP-I
SN08bh	0.060	0.015 (0.0001)	54543.5 (5.0)	17.92 (0.01)	0.194 (0.015)	6201 (478)	34.77 (0.16)	CSP-I
SN08br	0.255	0.011 (0.0001)	54555.7 (9.0)	17.81 (0.01)	0.103 (0.016)	2608 (507)	33.32 (0.38)	CSP-I
SN08bu	1.149	0.022 (0.0001)	54566.8 (5.0)	18.32 (0.03)	0.288 (0.045)	5517 (586)	34.90 (0.22)	CSP-I
SN08ga	1.865	0.015 (0.0001)	54711.8 (4.0)	17.18 (0.02)	-0.049 (0.022)	5714 (368)	34.11 (0.13)	CSP-I
SN08gi	0.181	0.024 (0.0001)	54742.7 (9.0)	17.87 (0.01)	-0.006 (0.016)	5949 (518)	34.83 (0.18)	CSP-I
SN08gr	0.039	0.022 (0.0001)	54766.5 (4.0)	17.41 (0.01)	-0.084 (0.016)	7259 (389)	34.76 (0.12)	CSP-I
SN08hg	0.050	0.018 (0.0001)	54779.7 (5.0)	18.48 (0.02)	0.069 (0.025)	4406 (642)	34.87 (0.29)	CSP-I
SN08if	0.090	0.013 (0.0001)	54807.8 (5.0)	16.47 (0.02)	-0.136 (0.028)	6805 (283)	33.75 (0.10)	CSP-I
SN09ao	0.106	0.012 (0.0001)	54890.7 (4.0)	16.93 (0.01)	0.340 (0.013)	5436 (346)	33.44 (0.13)	CSP-I
SN09bu	0.070	0.011 (0.0001)	54907.9 (6.0)	16.95 (0.01)	0.132 (0.009)	5619 (381)	33.70 (0.14)	CSP-I
SN09bz	0.110	0.011 (0.0001)	54915.8 (4.0)	16.91 (0.01)	-0.074 (0.012)	5647 (386)	33.83 (0.14)	CSP-I
8321	0.080	0.107 (0.001)	54353.6 (5.0)	21.25 (0.04)	-0.479 (0.069)	6838 (354)	38.83 (0.13)	SDSS
SN06gq	0.096	0.069 (0.0005)	53992.4 (3.0)	20.39 (0.04)	-0.143 (0.032)	4708 (725)	37.08 (0.31)	SDSS
SN06iw	0.137	0.030 (0.0005)	54010.7 (1.0)	18.73 (0.04)	0.061 (0.017)	6300 (317)	35.72 (0.11)	SDSS
SN06jl	0.504	0.055 (0.0005)	54006.8 (15.0)	19.46 (0.02)	0.053 (0.033)	6450 (410)	36.50 (0.14)	SDSS
SN06kn	0.194	0.119 (0.0005)	54007.0 (1.5)	21.19 (0.08)	-0.067 (0.106)	6218 (431)	38.27 (0.19)	SDSS
SN06kv	0.080	0.062 (0.0005)	54016.5 (4.0)	20.26 (0.05)	-0.072 (0.072)	5208 (383)	37.05 (0.17)	SDSS
SN07kw	0.074	0.067 (0.0005)	54361.6 (2.5)	19.96 (0.02)	-0.055 (0.027)	5854 (429)	36.93 (0.15)	SDSS
SN07ky	0.105	0.073 (0.0005)	54363.5 (3.0)	20.70 (0.03)	-0.080 (0.043)	5069 (356)	37.45 (0.15)	SDSS
SN07kz	0.320	0.127 (0.0005)	54362.6 (3.5)	21.54 (0.06)	-0.239 (0.092)	5981 (354)	38.70 (0.16)	SDSS
SN07lb	0.496	0.038 (0.0005)	54368.8 (7.0)	18.58 (0.01)	0.022 (0.013)	7550 (408)	35.91 (0.12)	SDSS
SN07ld	0.255	0.027 (0.005)	54369.6 (5.5)	18.19 (0.01)	-0.044 (0.009)	6264 (367)	35.26 (0.43)	SDSS
SN07lj	0.118	0.049 (0.005)	54370.2 (3.5)	19.69 (0.02)	-0.055 (0.027)	5796 (397)	36.64 (0.27)	SDSS
SN07lx	0.120	0.056 (0.0005)	54374.5 (8.0)	20.18 (0.03)	-0.039 (0.044)	5282 (413)	36.97 (0.17)	SDSS
SN07nr	0.079	0.139 (0.0005)	54353.5 (5.0)	22.20(0.12)	-0.383 (0.152)	5216 (327)	39.25 (0.22)	SDSS
SN07nw	0.204	0.056 (0.0005)	54372.2 (7.0)	20.42 (0.03)	0.042 (0.048)	6419 (736)	37.46 (0.23)	SDSS
SN07ny	0.080	0.142 (0.0005)	54367.7 (7.0)	21.81 (0.11)	-0.276 (0.162)	6379 (377)	39.11 (0.21)	SDSS
04D1pj	0.076	0.155 (0.0005)	53304.0 (8.0)	22.39 (0.04)	-0.052 (0.049)	6960 (332)	39.64 (0.12)	SNLS
04D4fu	0.072	0.132 (0.0005)	53213.0 (6.0)	22.36 (0.04)	-0.100 (0.04)	6166 (329)	39.46 (0.12)	SNLS
05D4dn	0.073	0.190 (0.0005)	53605.0 (7.0)	23.41 (0.08)	-0.079 (0.089)	5717 (860)	40.36 (0.32)	SNLS
06D1jx	0.079	0.134 (0.001)	54068.0 (6.0)	22.22 (0.02)	-0.088 (0.024)	5876 (392)	39.23 (0.14)	SNLS
06D2bt	0.051	0.079 (0.001)	53745.0 (10.0)	20.95 (0.03)	-0.078 (0.05)	5877 (416)	37.95 (0.16)	SNLS
SN2016fvh	0.052	0.341 (0.001)	57719.6 (2.0)	23.32 (0.04)	-0.162 (0.041)	9030 (452)	41.07 (0.12)	HSC